The Astrophysical Journal, 795:150 (13pp), 2014 November 10 doi:10.1088/0004-637X/795/2/150

ATMOSPHERIC CIRCULATION OF ECCENTRIC HOT JUPITER HAT-P-2B

Nikole K. Lewis[1,6], Adam P. Showman[2], Jonathan J. Fortney[3], Heather A. Knutson[4], and Mark S. Marley[5]
[1] Department of Earth, Atmospheric and Planetary Sciences, Massachusetts Institute of Technology, Cambridge, MA 02139, USA; nklewis@mit.edu
[2] Department of Planetary Sciences and Lunar and Planetary Laboratory, The University of Arizona, Tucson, AZ 85721, USA
[3] Department of Astronomy & Astrophysics, University of California, Santa Cruz, CA 95064, USA
[4] Division of Geological and Planetary Sciences, California Institute of Technology, Pasadena, CA 91125, USA
[5] NASA Ames Research Center 245-3, Moffett Field, CA 94035, USA
Received 2013 November 11; accepted 2014 September 15; published 2014 October 23

ABSTRACT

The hot Jupiter HAT-P-2b has become a prime target for *Spitzer Space Telescope* observations aimed at understanding the atmospheric response of exoplanets on highly eccentric orbits. Here we present a suite of three-dimensional atmospheric circulation models for HAT-P-2b that investigate the effects of assumed atmospheric composition and rotation rate on global scale winds and thermal patterns. We compare and contrast atmospheric models for HAT-P-2b, which assume one and five times solar metallicity, both with and without TiO/VO as atmospheric constituents. Additionally we compare models that assume a rotation period of half, one, and two times the nominal pseudo-synchronous rotation period. We find that changes in assumed atmospheric metallicity and rotation rate do not significantly affect model predictions of the planetary flux as a function of orbital phase. However, models in which TiO/VO are present in the atmosphere develop a transient temperature inversion between the transit and secondary eclipse events that results in significant variations in the timing and magnitude of the peak of the planetary flux compared with models in which TiO/VO are omitted from the opacity tables. We find that no one single atmospheric model can reproduce the recently observed full orbit phase curves at 3.6, 4.5 and 8.0 μm, which is likely due to a chemical process not captured by our current atmospheric models for HAT-P-2b. Further modeling and observational efforts focused on understanding the chemistry of HAT-P-2b's atmosphere are needed and could provide key insights into the interplay between radiative, dynamical, and chemical processes in a wide range of exoplanet atmospheres.

Key words: atmospheric effects – methods: numerical – planets and satellites: general – planets and satellites: individual (HAT-P-2b)

Online-only material: color figures

1. INTRODUCTION

HAT-P-2b (aka HD 147506b, $M_p = 8M_J$, $R_p = 1R_J$) was the among the first transiting extrasolar planets discovered to have a significant orbital eccentricity ($e \sim 0.5$; Bakos et al. 2007). Previous studies of the highly eccentric HD 80606b ($e \sim 0.9$) focused on orbital phases near the planet's periapse passage and secondary eclipse (when the planet passes behind its host star) to make the first determination of the radiative timescale at infrared wavelengths of an exoplanet atmosphere (Laughlin et al. 2009). However, the long duration of HD 80606b's orbit (111 days) makes it nearly impossible to observe the planet through the entirety of its orbit. HAT-P-2b has an orbital period just over 5.6 days (Bakos et al. 2007; Winn et al. 2007; Loeillet et al. 2008; Pál et al. 2010), which makes it an advantageous target for full-orbit observations to study the evolution of planetary flux with orbital phase.

The incident flux on HAT-P-2b from its stellar host at periapse is ten times that at apoapse, which should cause large variations in atmospheric temperature, wind speeds, and chemistry. We recently used full orbit *Spitzer* observations at 3.6, 4.5, and 8.0 μm of the HAT-P-2 system to measure HAT-P-2b's flux variations as a function of orbital phase and constrain the radiative timescale on the planet near periapse to be between two and eight hours (Lewis et al. 2013). Here we present three-dimensional atmospheric models for HAT-P-2b with a range of atmospheric compositions and rotation rates that can be compared directly to these observations. These atmospheric models for HAT-P-2b add to the growing body of work investigating the atmospheric dynamics of close-in Jovian sized planets, most of which focus on planets with circular orbits (e.g., Showman & Guillot 2002; Cooper & Showman 2005; Cho et al. 2008; Showman et al. 2009; Langton & Laughlin 2007; Dobbs-Dixon et al. 2010; Menou & Rauscher 2009; Rauscher & Menou 2010; Heng et al. 2011; Perna et al. 2012; Heng 2012; Showman et al. 2013; Rauscher & Menou 2013; Mayne et al. 2014).

Only a handful of studies have investigated the atmospheric circulation of eccentric "hot Jupiters" (Langton & Laughlin 2008; Lewis et al. 2010; Kataria et al. 2013). The simulations of HAT-P-2b presented here provide theoretical predictions for the expected variations in the planetary flux as a function of orbital phase under a range of model assumptions. These theoretical predictions can be compared directly with observational data to reveal the complex radiative, dynamical, and chemical processes in HAT-P-2b's atmosphere that may or may not be fully captured by current state-of-the-art general circulation models. Detailed study of planets subject to strong time-variable forcing such as HAT-P-2b present a unique opportunity to understand the competing effects of radiation, dynamics, and chemistry that shape the global circulation patterns of extrasolar planets.

In the following sections we first describe the set-up of our three-dimensional atmospheric model for HAT-P-2b (Section 2) including variations in the assumed atmospheric chemistry and rotation period for the planet. We present the results from our model simulations in Section 3 including the thermal structure and winds that develop in each case and the resulting theoretical light curves and spectra. In Section 4 we discuss the overall trends we see in our simulations of HAT-P-2b's atmosphere and

[6] Sagan Postdoctoral Fellow.

compare and contrast our model predictions with what has been observed. Finally, in Section 5 we present a summary of our results and discuss future work.

2. ATMOSPHERIC MODEL

We employ a three-dimensional coupled atmospheric radiative transfer and dynamics model, the Substellar and Planetary Atmospheric Radiation and Circulation (SPARC) model, to investigate the atmospheric circulation of HAT-P-2b. The SPARC model was developed specifically to explore atmospheric circulation on exoplanets and is described in detail in Showman et al. (2009) as applied to HD 189733b and HD 209458b, Lewis et al. (2010) as applied to GJ 436b, and Kataria et al. (2013) as applied to an HD 189733b-like planet on a range of eccentric orbits. The SPARC model employs the MITgcm (Adcroft et al. 2004) to treat the atmospheric dynamics and utilizes a two-stream variant of the non-gray radiative transfer model of Marley & McKay (1999) in order to realistically determine the magnitude of radiative heating/cooling at each grid point. The simulations presented here take advantage of the cubed-sphere grid (Adcroft et al. 2004) at a resolution of C16 (roughly 32×64 in latitude and longitude) to solve the relevant dynamic and energy equations. The vertical dimension in these simulations spans the pressure (p) range from 1000 bar to 0.2 mbar with 45 vertical levels, evenly spaced in $\log(p)$, and a top layer that extends to zero pressure.

Atmospheric opacities are computed according to Freedman et al. (2008) as a function of pressure, temperature, and wavelength assuming a range of atmospheric compositions in thermochemical equilibrium (Lodders & Fegley 2002, 2006). We then divide the full wavelength range into 11 wavelength/frequency bins for greater computational efficiency (see Kataria et al. 2013, for a full discussion of the 11 wavelength bin version of SPARC). Within each wavelength bin we utilize the correlated-k method (e.g., Mlawer et al. 1997; Goody et al. 1989; Fu & Liou 1992; Marley & McKay 1999) to determine the overall opacity using eight gauss points. This results in 88 separate radiative transfer calculations to determine upward and downward fluxes for a single grid point. It is important to note that this approach is far more accurate than simple band models (e.g., Dobbs-Dixon et al. 2012) and statistically incorporates information from several million wavelength points in each of our wavelength bins. Amundsen et al. (2014) have demonstrated the superiority of the correlated-k method compared to the mean-opacity method in their models of HD 209458b.

In this study, we consider atmospheric compositions of both one times ($1\times$) and five times ($5\times$) solar metallicity. In the $5\times$ solar metallicity case, the abundance of all elements besides hydrogen and helium are enhanced by five times standard solar values. Given HAT-P-2b's mass and radius it is possible that it is enriched in heavy elements (e.g., Fortney et al. 2008b; Guillot 2005). We also consider atmospheric compositions with and without TiO and VO. As proposed in Fortney et al. (2008a) (see also, Hubeny et al. 2003), the presence of the strong optical absorbers TiO and VO in a planet's atmosphere could be responsible for atmospheric temperature inversions that have been observed for a number of extrasolar planets. Here TiO and VO are assumed to be at their equilibrium abundances, depending on the local temperature and pressure, following Lodders (2002). The computed equilibrium abundances and corresponding opacities do account for rainout of condensed species (including TiO and VO). Although we do not rigorously treat possible "cold-trapping" (Hubeny et al. 2003), our opacity tables

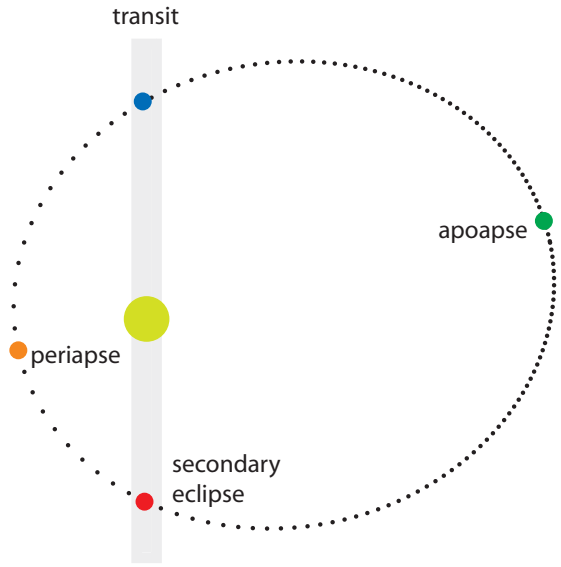

Figure 1. Orbit of HAT-P-2b assuming parameters from Lewis et al. (2013). Dots along the orbital path represent points where data was extracted to produce Figures 7, 9, and 11. The temporal interval between the points is one hour. Orbital motion is in the counterclockwise direction. Colored dots represent points near periapse (orange), transit (blue), apoapse (green), and secondary eclipse (red), which correspond to the colored spectra and pressure temperature profiles presented in Figures 9 and 11 respectively.

(A color version of this figure is available in the online journal.)

in which TiO and VO have been excluded represent a case where these chemical species have been cold trapped in the deep atmosphere (below 100 bars) or condensed out on the nightside of the planet (day/night cold trap) as suggested by the models of HD 209458b by Parmentier et al. (2013) and the observations of WASP-12b by Sing et al. (2013). Certainly it is possible for cold trapping to be incomplete, leaving TiO and VO at a few percent of their equilibrium abundance levels, but here we only consider the end-member state of complete TiO/VO removal.

In our model we assume the planetary and stellar parameters for the HAT-P-2 system given in Lewis et al. (2013). We assume a nominal rotation period of 1.9462563 days for HAT-P-2b, which we calculate using the pseudo-synchronous rotation relationship presented in Hut (1981). Additionally, we construct models with a rotation periods twice ($2\times$) and half ($0.5\times$) the nominal pseudo-synchronous rotation period for our standard $1\times$ solar composition model that includes TiO and VO. We initialize the model with wind speeds set to zero everywhere and each column of the grid assigned the same pressure–temperature profile. This initial pressure–temperature profile is derived from one-dimensional radiative-equilibrium calculations described in Fortney et al. (2005, 2008a) assuming no atmospheric dynamics and that HAT-P-2b is at the periapse of its orbit with an intrinsic effective temperature of 300 K. We find no difference in the equilibrated state of models initiated near apoapse with a one-dimensional pressure–temperature profile assuming the planet's apoapse distance as opposed to periapse with a one-dimensional pressure–temperature profile assuming the planet's periapse distance. This is in line with the results from Liu & Showman (2013), who found that the steady-state solution of hot Jupiter circulation models are insensitive to the initial conditions. The time-varying distance of the planet with respect to its host star, $r(t)$, is determined using Kepler's equation (Murray & Dermott 1999) and used to update the incident flux on the planet at each radiative timestep. A diagram of HAT-P-2b's orbit is presented in Figure 1.

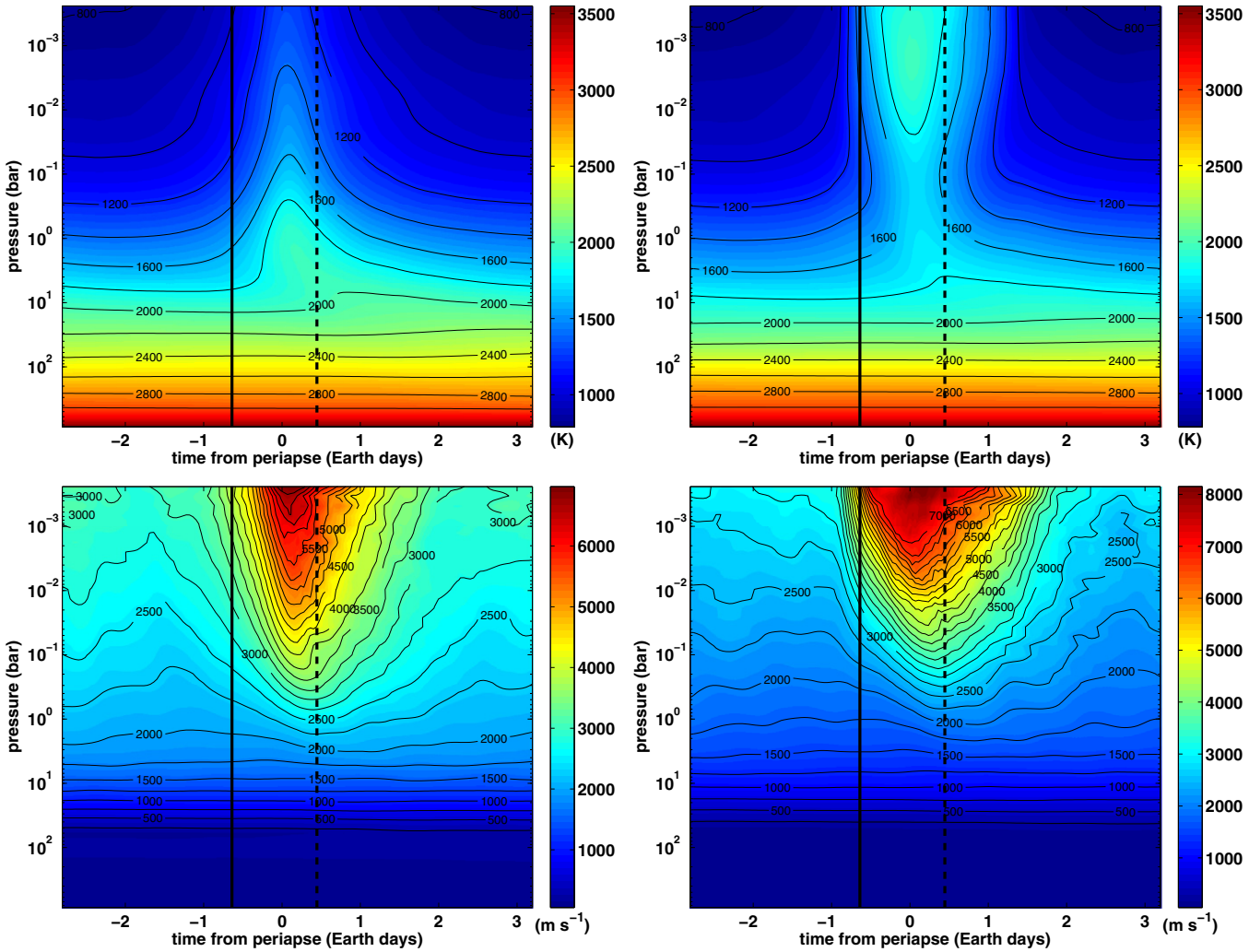

Figure 2. Horizontally averaged temperature (top) and rms horizontal velocity (bottom) as a function of time relative to periapse passage for our simulations without TiO/VO (left) and with TiO/VO (right). The temperatures represent averages over latitude and longitude as a function of pressure. rms horizontal velocities are calculated according to Equation (1). The times of transit and secondary eclipse are represented by the vertical solid and dashed lines respectively.
(A color version of this figure is available in the online journal.)

We solve for the relevant dynamic and energy equations using a dynamical timestep of 5 s. For computational efficiency, the radiative timestep used to update the radiative fluxes is varied as a function of orbital phase. We use a radiative timestep of 5 s, 25 s, and 50 s when the planet is near the periapse, midpoint, and apoapse of its orbit respectively. We apply a fourth-order Shapiro filter in the horizontal direction to both velocity components and the potential temperature over a timescale equivalent to the dynamical timestep in order to reduce small scale grid noise while minimally affecting the physical structure of the wind and temperature fields at the large scale. We integrate our model until the orbit averaged root-mean-square (rms) velocity given by

$$V_{\rm rms}(p) = \sqrt{\frac{\int (u^2 + v^2)\, dA}{A}} \quad (1)$$

where the integral is a global (horizontal) integral over the globe, A is the horizontal area of the globe, u is the east–west wind speed, and v is the north–south wind speed, reaches a stable configuration. Any further increases in wind speeds will be small and confined to pressures well below the mean photosphere so as not to affect any synthetic observations derived from our model atmosphere. For the simulations presented here the nominal integration time is ∼300 simulated days, which is equivalent to more than 50 planetary orbits. We find that the total angular momentum in our simulations varies by less than 0.1% and is hence well conserved.

3. RESULTS

3.1. Thermal Structure and Winds

Our atmospheric models of HAT-P-2b exhibit large variations in both temperature and wind speeds as a function of orbital phase. Figure 2 presents temperature, averaged over latitude and longitude, and rms velocity as a function of both pressure and simulated time for a single orbit of HAT-P-2b for our 1× solar models both with and without TiO/VO. Below the 10 bar level, average temperatures and wind speeds in our models are not strongly affected by the changes in incident flux on HAT-P-2b during its orbit and are similar between models with and without TiO/VO as an atmospheric constituent. Above the 1 bar level, both average temperature and wind speeds are a strong function of orbital phase and display marked difference between models that include TiO/VO and models in which TiO/VO has been excluded. This difference in global temperature and wind speeds in models with TiO/VO as compared to models without

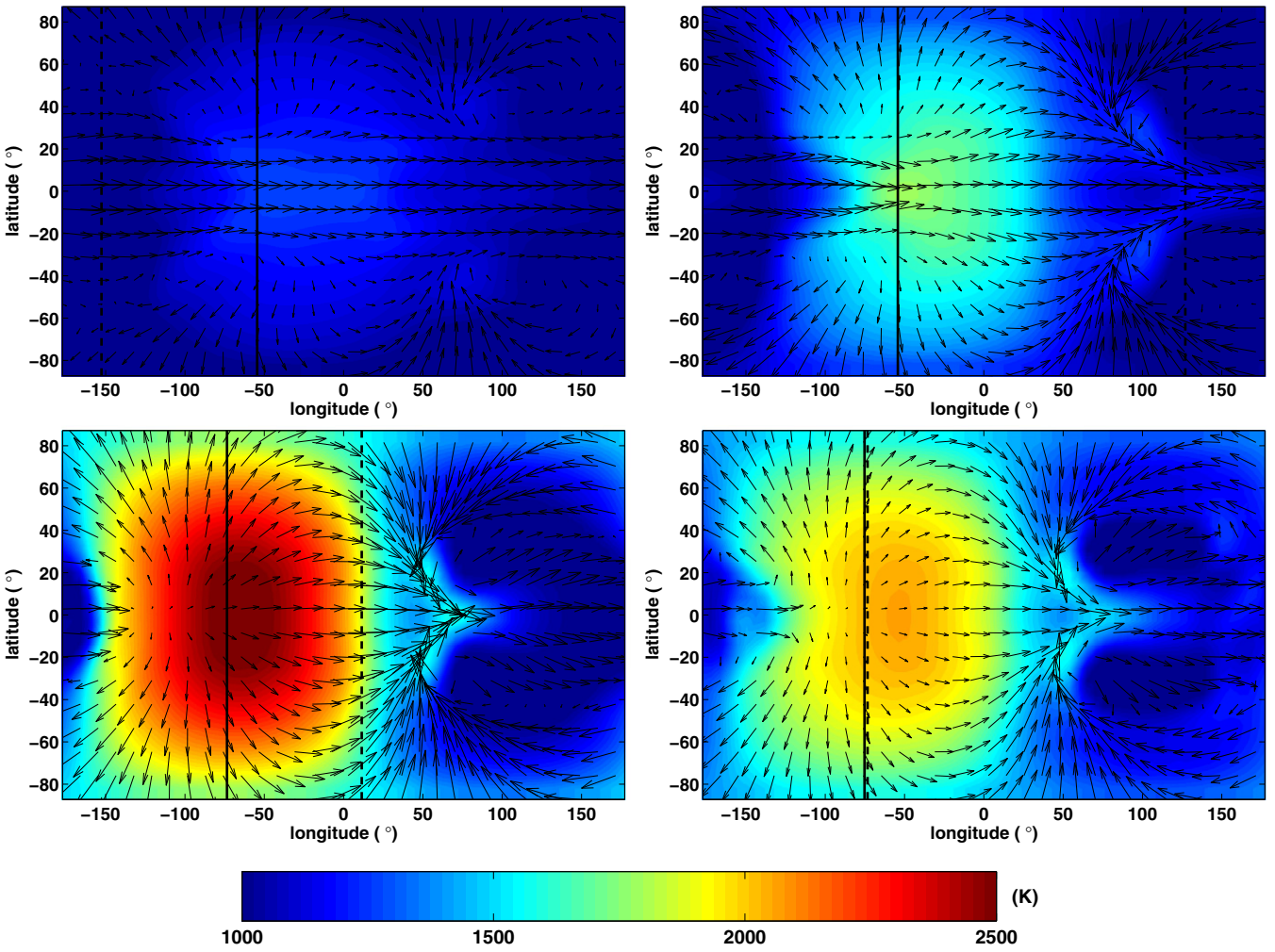

Figure 3. Temperature (colorscale) and winds (arrows) at the 100 mbar level of our 1× solar model without TiO/VO for time near apoapse (top left), transit (top right), periapse (bottom left), and secondary eclipse (bottom right). The longitude of the substellar and sub-Earth points are indicated in each panel by the solid and dashed vertical lines respectively. A substantial day/night temperature contrast exist for the majority of the HAT-P-2b's orbit in our models. The offset between the substellar longitude and the peak in the planet's temperature varies between ∼10° and ∼50° during the planet's orbit.

(A color version of this figure is available in the online journal.)

TiO/VO is the result of the development of a transient thermal inversion as seen in the top right panel of Figure 2.

The timing of the peak of global wind speeds and temperatures also varies between models that include TiO/VO and those that do not. We find that peak global temperatures above the 10 bar level occur ∼1 hr and ∼2 hr after periapse for the models with and without TiO/VO respectively. A similar variation in the timing of peak wind speeds above 1 bar is also seen with the peak occurring ∼3 hr after periapse for models with TiO/VO and ∼4 hr after periapse for models that do not include TiO/VO. It is also interesting to note that elevated wind speeds near periapse are much larger in magnitude and persist for a significantly longer time in our models with TiO/VO as compared to those models with out TiO/VO.

It is also important to note the timescales that we expect the increase and decrease in the planetary flux to occur over and how those timescales vary with pressure as they will shape the observed phase curves. At all pressures, the timescales required for the planet to heat up are shorter than those required for the planet to cool down. This means that we expect HAT-P-2b's temperature to remain elevated above pre-periapse levels well into the apoapse of its orbit and a minimum in the planetary flux to occur sometime between apoapse and transit. The slope of the planetary cool-down period greatly increases with increasing pressure. By comparing the cool-down timescales measured by the phase-curves at various wavelengths, rough constraints can be placed on the pressure levels being probed by each bandpass.

3.1.1. Evolution of Thermal and Wind Patterns

In addition to changes in average temperature, it is important to consider day/night temperature contrasts that can also affect the observed planetary flux as a function of orbital phase. Figures 3 and 4 presents slices from our 1× solar model without and with TiO/VO, respectively. These slices are from the 100 mbar level of our simulations, which is near the predicted infrared photosphere of the planet, and represent snapshot near the apoapse, transit, periapse, and secondary eclipse events of HAT-P-2b's orbit. The basic winds patterns that develop at the 100 mbar level are very similar between the simulations with and without TiO/VO, at all orbital phases. The key differences between the simulations with and without TiO/VO is the magnitude of thermal gradient between the day and night sides of the planet that results from the dayside thermal inversion that develops in the simulations that include TiO/VO.

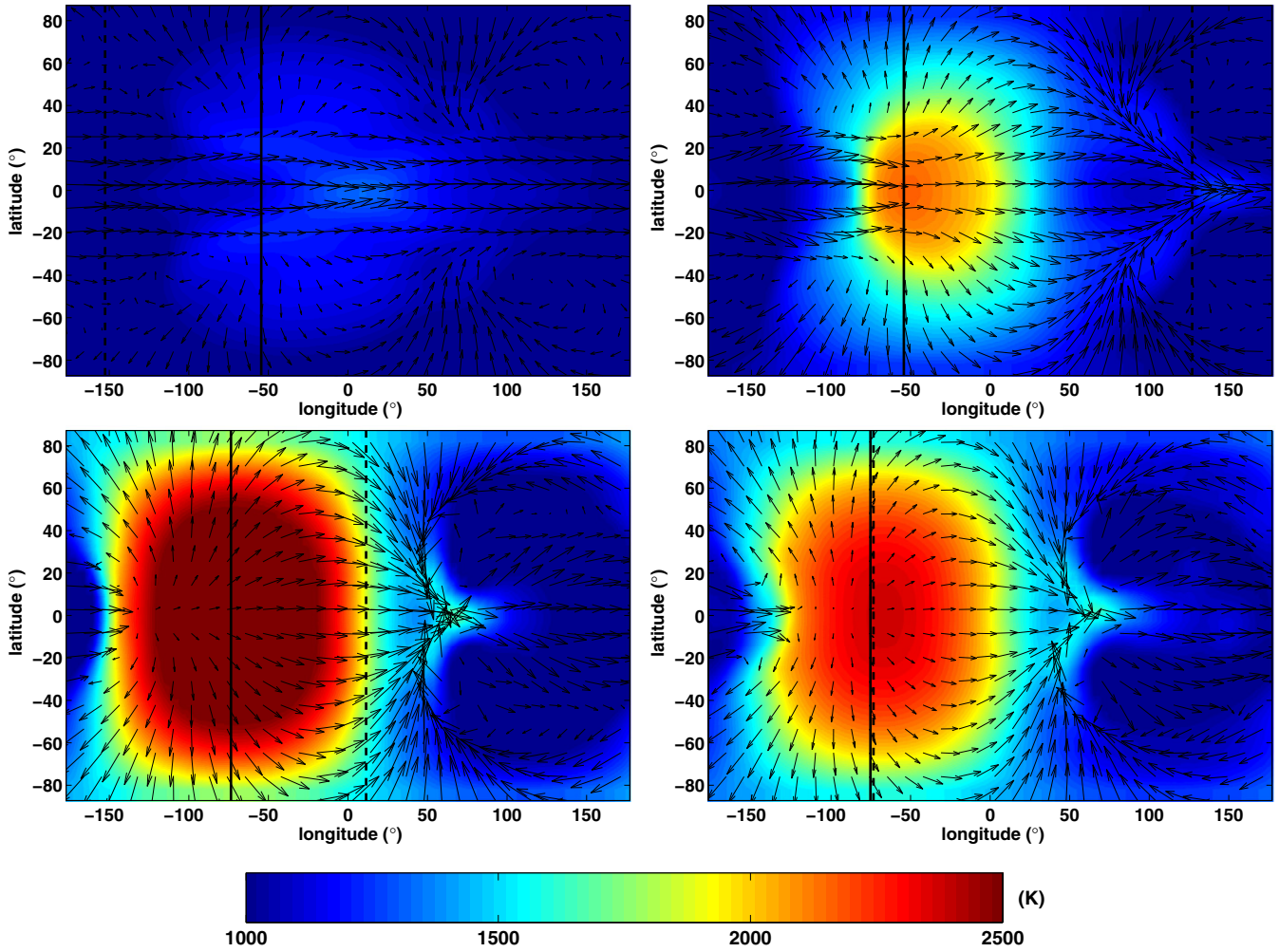

Figure 4. Temperature (colorscale) and winds (arrows) at the 100 mbar level of our 1× solar model with TiO/VO for time near apoapse (top left), transit (top right), periapse (bottom left), and secondary eclipse (bottom right). The longitude of the substellar and sub-Earth points are indicated in each panel by the solid and dashed vertical lines respectively. A substantial day/night temperature contrast exist for the majority of the HAT-P-2b's orbit in our models. The offset between the substellar longitude and the peak in the planet's temperature varies between ∼0° and ∼20° during the planet's orbit.

(A color version of this figure is available in the online journal.)

We find that a significant day/night temperature contrast exists in our simulations at pressures less than 10 bar for the majority of HAT-P-2b's orbit. Temperature differences between the day and night side hemispheres are greatest near the periapse and weakest near apoapse. This is not surprising given that changes in radiative timescales can be related to atmospheric temperatures (T) by $\tau_{\rm rad} \propto T^{-3}$. Even in the presence of strong winds, or other dynamical processes such as wave propagation, significant horizontal temperature contrasts will exist if $\tau_{\rm rad} \ll \tau_{\rm dyn}$, where $\tau_{\rm dyn}$ is the relevant dynamical timescale (Showman et al. 2010; Perez-Becker & Showman 2013). It is important to note that $\tau_{\rm dyn}$ does not vary as strongly with temperature as $\tau_{\rm rad}$ and will therefore vary more mildly throughout HAT-P-2b's orbit. We find that near the 100 mbar level of our simulations at periapse passage $\tau_{\rm rad} < 1$ hr and $\tau_{\rm dyn} \sim 10$ hr, which results in a large day-night temperature contrast during this phase of HAT-P-2bs orbit. As HAT-P-2b approaches apoapse, $\tau_{\rm rad}$ grows to be on the order of 5–6 hr while $\tau_{\rm dyn}$ changes very little, which results in some muting of the day-night temperature difference. This qualitatively explains the variations in the day/night temperature difference throughout the orbit of HAT-P-2b seen in Figures 3 and 4.

An important regime shift in the global jet structure occurs as HAT-P-2b goes from the periapse to the apoapse of its orbit. At periapse, HAT-P-2b receives an amount of stellar insolation equivalent to that received by the "very-hot" Jupiter HAT-P-7b in its circular orbit. At these high effective temperatures ($T_{\rm eff} \sim 2400$ K) the formation of an equatorial jet is suppressed and instead air heated near the substellar point flows uniformly outward toward the day/night terminator, forming a "day-to-night" circulation pattern (see bottom panels in Figures 3 and 4). The jet suppression is due to the fact that the radiative timescales at these high temperatures are much shorter than the time required for the Kelvin and Rossby waves that drive the super-rotating (eastward) equatorial jet to propagate a planetary radius (Showman & Polvani 2011; Showman et al. 2013).

Near apoapse, the amount of incident stellar flux received by HAT-P-2b is similar to that received by the well-studied non-eccentric transiting hot-Jupiter HD 189733b. A number of both theoretical (e.g., Showman et al. 2009; Rauscher & Menou 2013) and observational (e.g., Knutson et al. 2007, 2012) studies have sought to understand the atmospheric circulation regime of HD 189733b. The consensus among both modelers and observers is that a super-rotating equatorial jet exists in

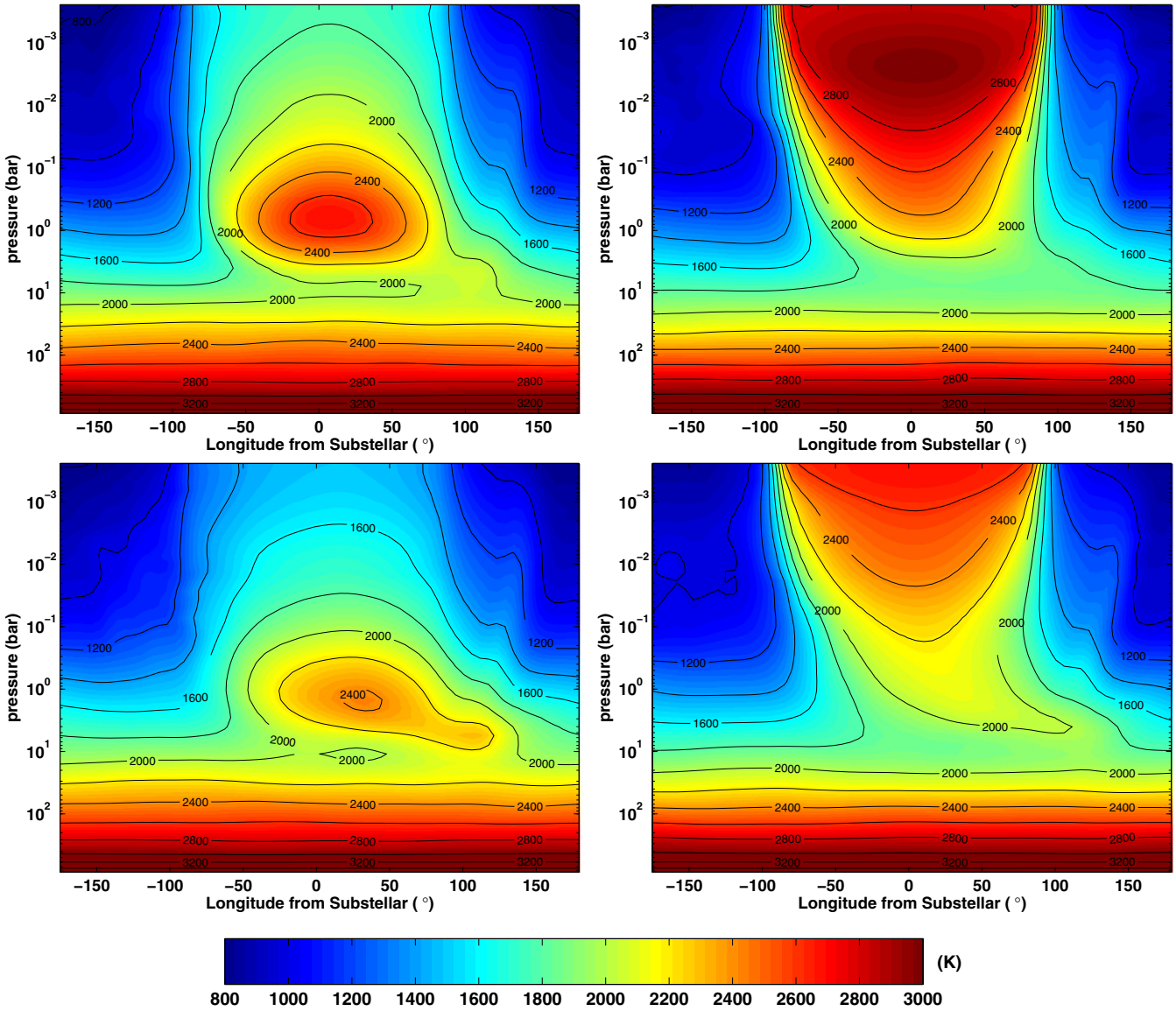

Figure 5. Temperature averaged in latitude (colorscale) as a function of pressure and degrees from the substellar longitude at periapse (top) and secondary eclipse (bottom) from our models with (right) and without (left) TiO/VO. Temperatures represent average values weighted by $\cos(\phi)$, where ϕ is latitude. Note how the location of the hottest point on the planet evolves between the periapse and secondary eclipse events and differs significantly between models with and without TiO/VO.

(A color version of this figure is available in the online journal.)

HD 189733b's atmosphere, which causes an overall shift in the observed thermal pattern of the planet of ∼30° to the east of the substellar longitude. The theory behind the formation of this super-rotating jet is well described in Showman & Polvani (2011). We see a similar eastward jet form near the equator in our HAT-P-2b simulations away from periapse (see top panels in Figures 3 and 4). Our simulations predict that the variations in the incident flux on the planet due to its eccentric orbit causes it to shift between the jet dominated and day–night flow dominated regimes identified in Showman et al. (2013).

3.1.2. Equatorial Hot Spot

In our simulation we see an interesting interplay between radiative and advective timescales that causes the displacement of the hottest point on the planet, or hotspot, from the substellar point to evolve with orbital phase. Figure 5 shows the temperature, averaged in latitude, as a function of pressure and longitude from the substellar point near periapse and secondary eclipse for our 1× solar models both with and without TiO/VO. A clear difference between those models that have TiO/VO and those that do not is the pressures at which the hot spot predominately resides. In our case without TiO/VO the hot spot is generally centered around the 1 bar level while our models with TiO/VO have a hot spot centered between 1 and 10 mbar. This decrease in the pressure level of the hot spot is due to the fact that TiO and VO absorb incoming visible wavelength starlight at lower pressures, thus creating a thermal inversion and the vertical shift in the hot spot seen in Figure 5.

Above the 10 bar level in our models near periapse (Figure 5), we see that the hot spot in the models without TiO/VO is offset from the substellar point by about 12° while the hot spot is offset from the substellar point by less than 5° in our models with TiO/VO. Although wind speeds are much greater in our models with TiO/VO (Figure 2), radiative timescales are much

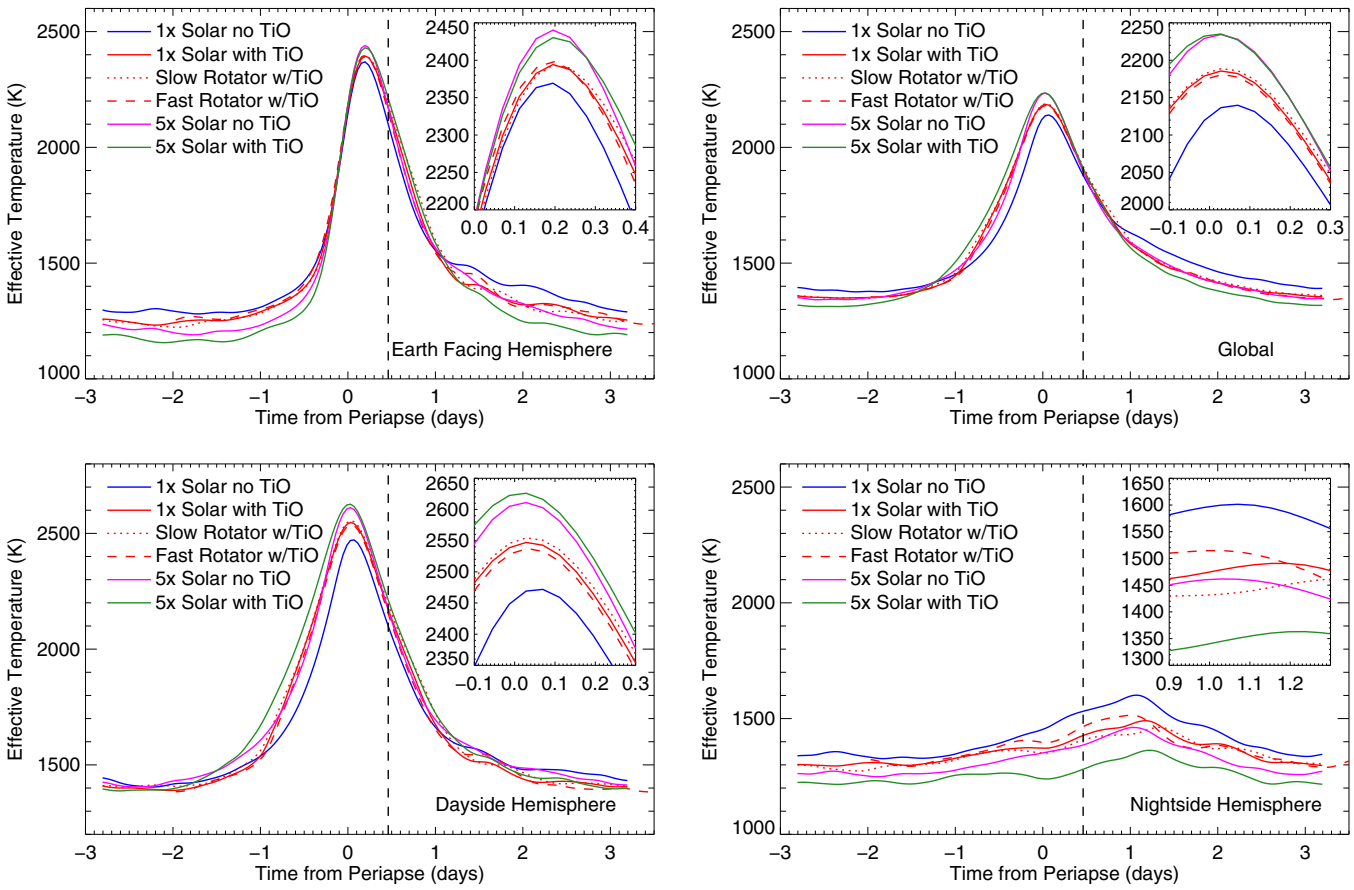

Figure 6. Effective temperature as a function of time from periapse passage for the Earth-facing hemisphere (top left), entire planet (top right), dayside hemisphere (bottom left), and nightside hemisphere (bottom right) for each of the simulations considered here. Insets provides a detailed view of the peak in effective temperature for each case, which highlights the difference in the magnitude and offset of the peak in planetary flux between each of the simulations. Dashed vertical line in each panel represents the temporal location of secondary eclipse.

(A color version of this figure is available in the online journal.)

shorter compared to models that do not include TiO/VO due to the pressure levels at which the hot spot develops. This means that parcels of air cool more rapidly than they can be advected downwind in our cases with TiO/VO, which result in a smaller offset in the hot spot compared to models that do not include TiO/VO.

We also observe that the magnitude of the hotspot offset increases dramatically in the pressure region between 1 and 10 bar as the planet goes from perhaps to secondary eclipse. This increase in the hotspot offset as a function of orbital phase occurs in both simulations with and without TiO/VO. It is in the 1 to 10 bar region of the atmosphere that radiative and advective timescales become similar and the efficient transport of "heat" deposited near periapase away from the substellar point can occur. Wavelengths that probe this deep pressure region may show a pronounced offset in the peak of the thermal phase curve away from secondary eclipse and toward periapse given the geometry of the HAT-P-2 system. This shift in the hot spot highlights the importance of self-consistent treatment of three-dimensional radiative and advective processes in atmospheric models for exoplanets, especially those on eccentric orbits.

3.2. Theoretical Light Curves and Spectra

The SPARC model is uniquely equipped to produce both theoretical light curves and spectra directly from our three-dimensional atmospheric model for HAT-P-2b. Once our simulations for HAT-P-2b reach an equilibrium state, we record pressure and temperature profiles along each grid column at many points along the planet's orbit (Figure 1). These pressure–temperature profiles are then used in high resolution spectral calculations to determine the emergent flux from each point on the planet and which portion of that emergent flux would be directed toward an Earth observer including limb darkening/brightening effects. Spectra and light curve generation methods are fully described in Fortney et al. (2006).

The three-dimensional nature of our models also allows us to invoke any number of viewing angles and wavelength ranges in determining the theoretical emission from as a function of time. In Figure 6 we present the effective temperature of the Earth-facing hemisphere, dayside, and global average as a function of time from periapse passage. The effective temperature of a hemisphere is calculated by integrating the planets emitted spectrum over all wavelengths from a particular viewing location such as Earth or the parent star, to obtain the total flux from the hemisphere. This quantity is then divided by the Stefan–Boltzmann constant, σ, and the fourth root it taken to obtain a temperature. For the global effective temperature calculation, the flux from both hemispheres (e.g., for day and night, far above the substellar point and anti-stellar point, respectively) are first added together before a temperature is determined.

The effective temperatures presented in Figure 6 provide important insights into the planetary response to the variations in

heating experienced by HAT-P-2b throughout its orbit from our various models. The effective temperatures for the Earth-facing hemisphere clearly show a trend between the magnitude of the peak effective temperature and the time lag between periapse passage and when the peak in temperature occurs. This trend is predominately the result of the orbital geometry of the HAT-P-2 system as the opposite trend in peak timing and magnitude can be seen in the dayside effective temperatures in the bottom left panel of Figure 6. The trend in the dayside hemisphere effective temperatures results from opacity differences between the models that exist because of changes in the dayside thermal structure and composition based on our equilibrium chemistry assumptions. As can been seen in the evolution of the nightside effective temperature as a function of time from periapse passage, those models that exhibit the greatest dayside effective temperatures also have the lowest nightside effective temperatures, which is the result of "inefficient" day-to-night heat transport at photospheric pressures. Interestingly, the only clear deviations between the effective temperatures of the nominal 1× solar with TiO case and its fast and slow rotating counterparts are seen in the nightside effective temperature as a function of orbital phase. It is important to keep in mind that the assumed nominal rotation period of HAT-P-2b is ∼1.95 days and that the timing of the peak in the nightside effective temperature is not just the result of the region heated at periapse rotating onto the nightside hemisphere. Instead the timing in the peak nightside temperature is the result of the evolution of the planet's thermal and wind structure as discussed in Section 3.1.1.

Figure 7 shows our theoretical light curves, expressed as a planet/star flux ratio as a function of time from periapse passage, compared with the observed *Spitzer* light curves at 3.6, 4.5, and 8.0 μm. The strong peaks that we see in our theoretical light curves is the result of a combination of intense heating at periapse and the offset (or lack thereof) of the hotspot from the substellar longitude. If HAT-P-2b's thermal structure did not vary with orbital phase and there were no shift in the hotspot from the substellar longitude, then we would expect the peak of the light curve to occur near secondary eclipse. As shown in Figure 5, the hot spot in HAT-P-2b's atmosphere is shifted eastward from the substellar longitude in both the cases with and without TiO/VO. This shift in the hot spot means that the hottest portion of the planet will rotate into view a few hours (∼2 hr) before secondary eclipse (∼8–11 hr after periapse passage). The timing of the peaks of our theoretical light curves represents an average value that lies between the peak determined by radiative timescales and the peak determined by dynamical timescales (orbital geometry, rotation, and winds).

It is clear that significant differences exist between the various model light curve predictions and between the observations and the model light curve predictions as a whole. The light curve predictions from models that include TiO/VO are fairly insensitive to variations in both composition (1× versus 5× solar metallicity) and rotation rate (0.5× and 2× nominal rotation period). Models that do not include TiO/VO, and therefore do not have a strong dayside inversion near periapse, give theoretical light curves that underestimate the planetary flux during the majority of planetary orbit at 3.6, 4.5, and 8.0 μm, especially in the region near periapse. It is important to note that if phase curve observations of HAT-P-2b were made in only one bandpass, that entirely different conclusions about the properties of the planet's atmosphere would be drawn. For example, if the 3.6 or 8 μm observations were taken on their own, or even combined, a comparison with the theoretical phase curves would

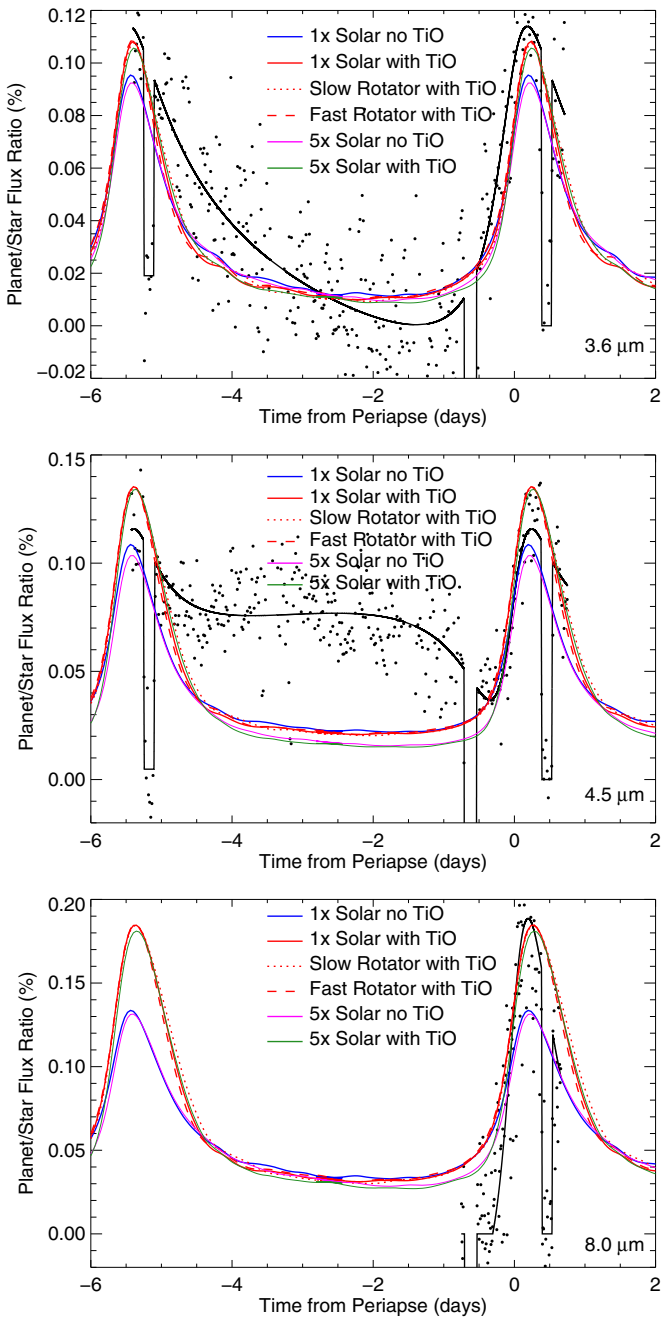

Figure 7. Theoretical planet/star flux ratio as a function of time from periapse for the 3.6 (top), 4.5 (middle), and 8.0 μm (bottom) *Spitzer* bandpasses compared with the observed light curves from Lewis et al. (2013). The observations have been binned into 20 minute intervals. For clarity, the solid black lines show the best-fit phase curves from Lewis et al. (2013).

(A color version of this figure is available in the online journal.)

strongly favor a scenario with a solar, or slightly super-solar, composition atmosphere in chemical equilibrium with a dayside thermal inversion, possibly caused by the presence of TiO/VO. However, the 4.5 μm observations do not conform particularly well to any of the theoretical light curves from our various models. This points to some physical process that is currently missing from our models and highlights the importance of multi-wavelength observations when constraining the properties of exoplanet atmospheres.

The amplitude (difference between maximum and minimum of planetary flux) of the phase curves along with the

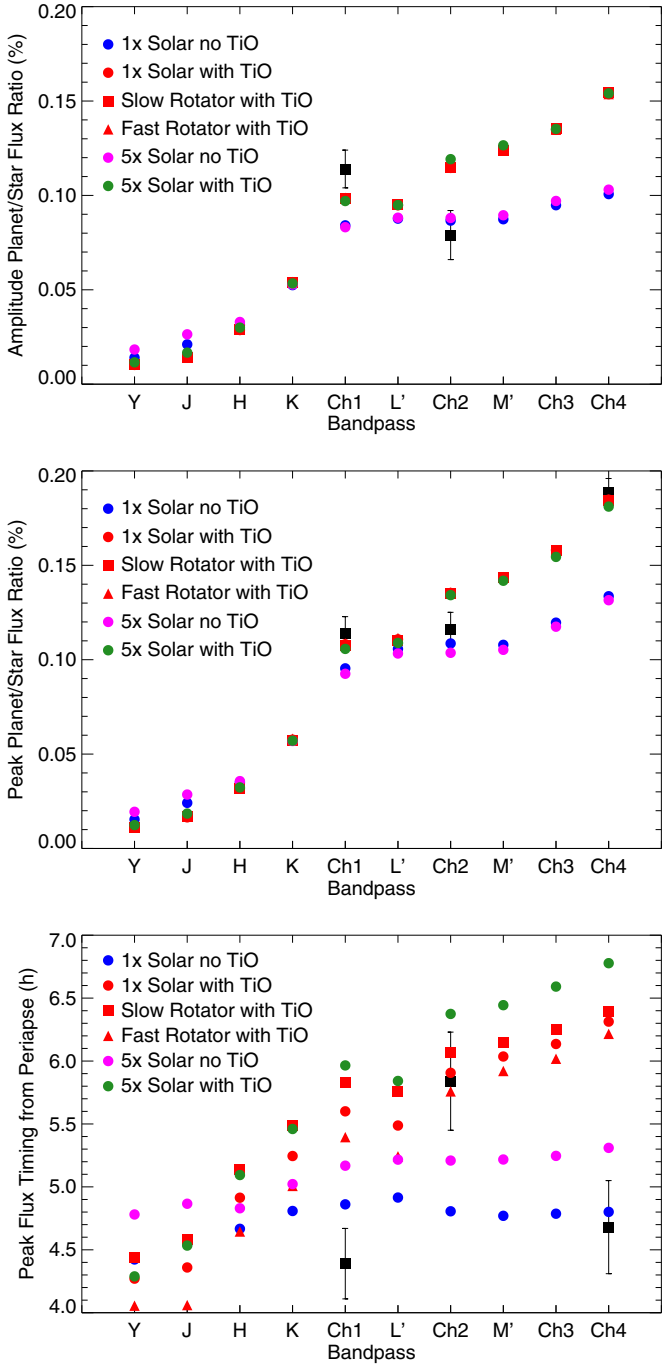

Figure 8. Amplitude (top), peak (middle), and timing of the peak (bottom) of the planet/star flux ratio as a function of bandpass. *Ch1*, *Ch2*, *Ch3*, and *Ch4* represent the 3.6, 4.5, 5.8, and 8.0 μm bandpasses of the *Spitzer* IRAC instrument respectively. The ground-based *Y*, *J*, *H*, *K*, *L*′, and M′ bandpasses have central wavelengths of 1.02, 1.26, 1.62, 2.21, 3.78, and 4.78 μm respectively. Observed values with one sigma error bars from Lewis et al. (2013) are over plotted with the black squares.

(A color version of this figure is available in the online journal.)

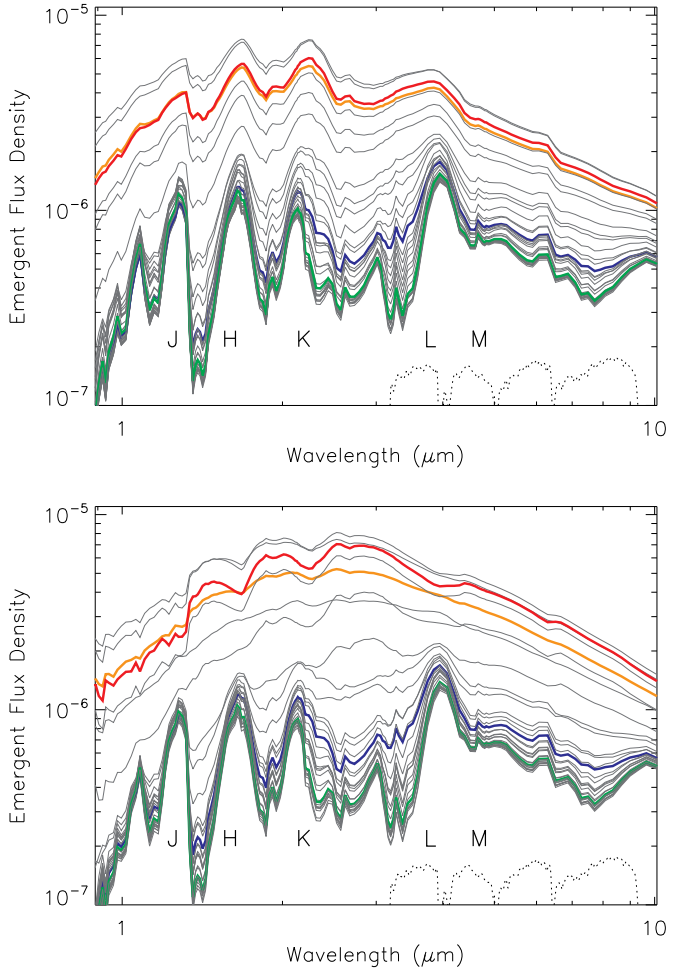

Figure 9. Flux per unit frequency, F_ν (erg s^{-1} cm^{-2} Hz^{-1}), as a function of wavelength for our solar metallicity atmospheric model of HAT-P-2b with (bottom) and without (top) TiO/VO. The spectra are taken from a subset of points along a single orbit as indicated in Figure 1. The central wavelengths of *J*-, *H*-, *K*-, *L*-, and *M*-bandpasses are indicated by their corresponding letters. Dotted lines at the bottom indicate the bandpasses of the four *Spitzer* IRAC bands from 3–9 μm. Colored spectra are taken near secondary eclipse (red), periapse (orange), transit (blue), and apoapse (green). Note how the absorption features in the spectra from the model with TiO/VO change to emission features as the planet approaches periapse.

(A color version of this figure is available in the online journal.)

maximum planetary flux value and the timing of that maximum from periapse reveal a great deal about atmospheric radiative and dynamical timescales in an eccentric planet's atmosphere. Figure 8 shows how these key phase curve parameters vary as a function of bandpass and model parameters and compares them with the values derived for the 3.6, 4.5, and 8.0 μm *Spitzer* light curves from Lewis et al. (2013). There is a clear divergence between models that incorporate TiO/VO into the opacity tables and those that do not, especially at longer wavelengths. It is also interesting that varying the rotation rate of the planet by a factor of two only results in small changes in the timing and shape of the peak in the planetary flux. Given the one sigma error bars from the *Spitzer* observations, it is impossible to distinguish the slow and fast rotation period models from the nominal pseudo-synchronous rotation period model. This highlights that atmospheric radiative timescales and the viewing geometry of the system predominately determine the shape of HAT-P-2b's phase curve.

If we plot the thermally emitted flux from the Earth-facing hemisphere of HAT-P-2b as a function of wavelength (Figure 9) a number of features are readily apparent. Most notably, the fluxes at secondary eclipse (red) and periapse (orange) are similar. While the planet is hotter at periapse than at secondary eclipse, at periapse we do not see the fully illuminated hemisphere. The black lines are spaced evenly in time throughout the orbit demonstrating that the planet spends most of its time at larger orbital separations where the thermal emission is weaker.

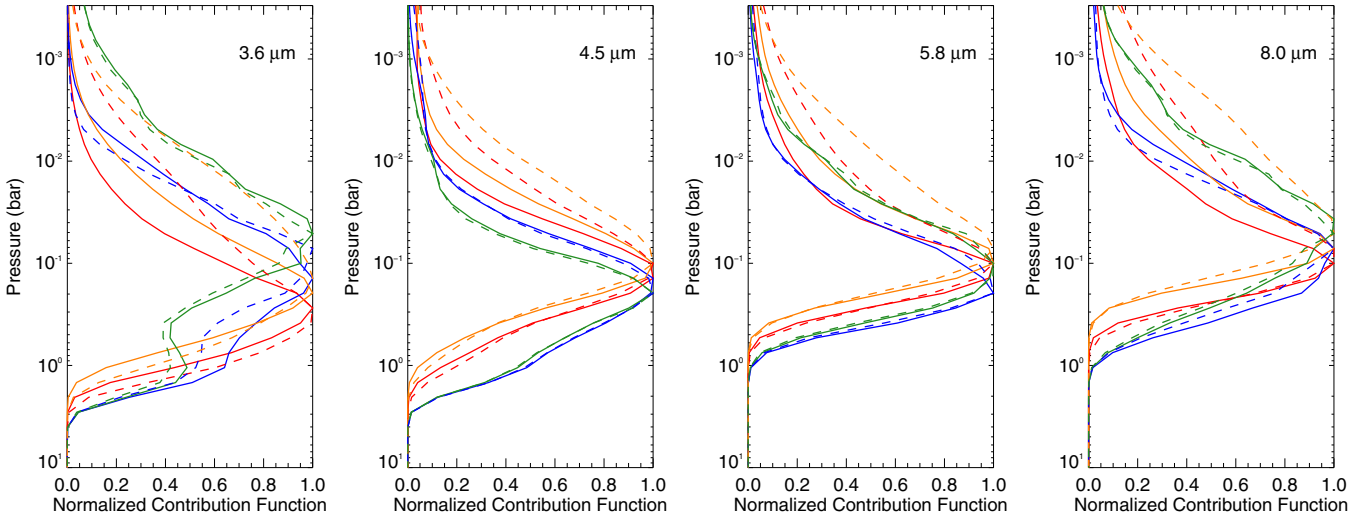

Figure 10. Normalized contribution of each pressure level in our 1× solar models to the 3.6, 4.5, 5.8, and 8.0 μm planetary flux at periapse (orange), secondary eclipse (red), apoapse (green), and transit (blue). Solid lines are for our model that did not incorporate TiO/VO into the opacity tables, while the dashed lines are for our model that did include TiO/VO.

(A color version of this figure is available in the online journal.)

One of the key advantages of the SPARC model is that we can consider how the contribution of flux from a given pressure level in our model might evolve with the planet's orbit (e.g., Knutson et al. 2009). This is especially important for planets on eccentric orbits where large changes in incident flux and atmospheric chemistry of the planet are expected. Figure 10 shows the normalized contribution function of the emitted planetary flux at transit, periapse, secondary eclipse, and apoapse for each of the *Spitzer* IRAC bandpasses. These contribution functions are computed from a single pressure temperature profile that represents an average over the visible hemisphere of the planet that is weighted by the viewing angle (see Fortney et al. 2006 for a discussion of the viewing angle).

It is important to note how the pressure levels probed by a given bandpass evolves with orbital phase and the difference in the contribution functions between models that include TiO/VO and those that do not (Figure 10). The evolution of the 3.6 μm contribution functions compared with the 4.5 μm contribution highlights changes in the relative abundances of CO and CH_4 in our models of HAT-P-2b's atmosphere as a function orbital phase and global temperatures. The 4.5 μm bandpass probes the absorption features from CO in the ∼4.5–5.0 μm range while the 3.6 μm bandpass probes the strong absorption feature from CH_4 at 3.3 μm. Differences between the pressures probed by models with and without TiO/VO in their atmospheres is, not surprisingly, strongest near periapse/secondary eclipse and enhances the contribution from lower pressure levels where the temperature inversion occurs and the planetary hot spot is well aligned with the substellar longitude (Figure 5). We expect the orbital variations in the contribution functions presented here will be reduced by chemical quenching (Cooper & Showman 2006; Visscher 2012), which is not currently accounted for in our models.

3.3. Variability

Typically when predicting the theoretical flux from the planet as a function of orbital phase from our three-dimensional simulations, we only consider a temporally averaged planetary thermal structure, or in the case of planets on eccentric orbits, the thermal structure of the planet that develops during a single orbit. As discussed in Showman et al. (2009) in the case of HD 189733b, orbit-to-orbit and longer term variations in an exoplanet's thermal structure are expected due to global scale oscillation and smaller scale turbulent processes. Langton & Laughlin (2008) noted large variations in the thermal structure of their two-dimensional simulations of HAT-P-2b, but did not quantify how these thermal variations might manifest themselves observationally from one epoch to the next. In Table 1, we present the variations in the predicted eclipse depth as a function of bandpass from our nominal solar metallicity simulation that does not include TiO/VO. These variations were calculated over a 100 simulated day period after the simulation had reached a stable configuration and include 24 estimates of the eclipse depth.

A clear trend in the data presented in Table 1 is that the expected level of eclipse depth variability is strongly correlated

Table 1
HAT-P-2b Secondary Eclipse Depth Variability

Bandpass[a]	λ[b] (μm)	σ[c]	Δ_{max}[d]	$\overline{P}_{band}$[e] (bar)
Y	1.02	5.4%	29.6%	2.13
J	1.26	4.6%	25.0%	1.75
H	1.62	2.1%	12.2%	0.78
K	2.21	1.0%	4.5%	0.40
Ch1	3.6	0.8%	3.5%	0.33
L′	3.78	0.9%	3.7%	0.12
Ch2	4.5	0.6%	2.5%	0.18
M′	4.78	0.6%	2.5%	0.05
Ch3	5.8	0.6%	2.7%	0.11
Ch4	8.0	0.6%	2.8%	0.09

Notes.
[a] *Ch1*, *Ch2*, *Ch3*, and *Ch4* represent the four *Spitzer* IRAC bandpasses. *Y*, *J*, *H*, *K*, *L′*, and *M′* represent standard near- to mid-infrared bandpasses used at ground-based observatories.
[b] Central wavelength of each bandpass.
[c] Standard deviation of the theoretical eclipse depths normalized to the mean.
[d] Maximum deviation in the theoretical eclipse depths normalized to the mean.
[e] Average pressure probed by each bandpass as determined from the relevant contribution functions (see Figure 10).

with wavelength. At the longer infrared wavelengths, the level of variability in the predicted eclipse depth is expected to be on the order of ∼1%. This is in line with the estimates for HD 189733b's eclipse depth variability at 8 μm presented in Showman et al. (2009). At the shorter infrared wavelengths, the predicted variability in the eclipse depth grows reaching between 5% and 10%. The level of variability in our simulations is also strongly correlated with the average pressure level probed by a given bandpass (last column Table 1). At depth in an exoplanet atmosphere, the radiative and dynamical (including wave phenomenon) timescales grow longer and become commensurate with the planetary orbital/rotational period near the 1 bar level of the atmosphere (Showman et al. 2008). This means that variations in the thermal structure can develop on periods greater than the orbital period leading to a greater level of predicted variability in the secondary eclipse depth at shorter wavelengths. We do not note any coherent oscillations in the predicted eclipse depth, but these oscillations may be at timescales less than an orbital period or greater than 24 orbital periods and would therefore not be readily apparent in our current analysis. Although we only present estimates of eclipse variability from our solar metallicity simulation that does not include TiO/VO, we expect the same general trend of variability increasing with pressure probed by a given bandpass for all of our simulations and cloud-free exoplanet atmospheres in general.

4. DISCUSSION

In the previous section we have outlined the basic thermal and wind structures that develop in our atmospheric models for HAT-P-2b. We have also compared theoretical light curves derived from our models to the observed light curves at 3.6, 4.5, and 8.0 μm from Lewis et al. (2013). In Lewis et al. (2013), we investigated the range of radiative and advective timescales that would explain the magnitude and timing in the of the peak in the planetary flux using the semi-analytic model of Cowan & Agol (2011). The models presented here support our predictions from Lewis et al. (2013) that radiative timescales are short (∼2 hr) and zonal wind speeds are large (∼4–5 km s^{-1}) for HAT-P-2b near the periapse of its orbit as determined using the simplified models of Cowan & Agol (2011). Our three-dimensional simulations allow us to more rigorously explore the interconnectivity between radiative and advective processes and provide additional context for the physical origin of phase curve variations we observe and predict for HAT-P-2b.

We can compare the amplitude, magnitude, and timing of the peak in the planetary flux from our models in much the same way as was done in Lewis et al. (2013) using the Cowan & Agol (2011) models. From Figure 8 it is clear that no one model provides the "best-fit" to the data and that at the three-sigma level most of our model predictions agree with the basic observed properties of the HAT-P-2b phase curve. The observed peak flux at 8.0 μm (Ch4) is the only point that strongly favors models that have an atmospheric inversion due to the presence of TiO/VO versus those models that do not include TiO/VO. Interestingly, the 8.0 μm peak flux timing more strongly favors those models without an inversion, but it is possible that the exact timing of the peak of the flux may be more strongly influenced by the timescales for vertical and horizontal mixing of TiO/VO, which are not rigorously accounted for in this study. Although our models seem to capture the correct heating timescales observed at 3.6 and 4.5 μm, they underestimate the cooling timescale of the planet at 3.6 and 4.5 μm (Figure 7). At 8 μm our models overestimate both the heating and cooling timescales of the planet. These discrepancies between the observed and modeled heating/cooling timescales point to changes in the pressure levels probed by each bandpass that are likely due to opacity (chemical) changes not captured by our model.

What is perhaps most striking when comparing our model light curves with the observed light curves (Figure 7) is that during certain orbital phases our atmospheric models significantly underestimate or overestimate the planetary flux. Our models tend to overestimate the planetary 4.5 μm flux near periapse (in the cases with TiO/VO) and underestimate the planetary flux for the bulk of the planetary orbit outside of periapse. At 3.6 μm, our atmospheric models show deviations from the observations in the opposite sense from what was observed at 4.5 μm, with the planetary flux slightly underestimated near periapse and overestimated near apoapse. Especially near apoapse where the planet cools, this discrepancy between our observations and our atmospheric models could suggest an enhancement of CH_4 and a depletion of CO compared with predicted solar metallicity equilibrium abundances. If the mixing ratio of CH_4 is increased in HAT-P-2b's atmosphere near apoapse, the amount infrared flux emitted by the planet at 3.6 μm will be greatly reduced, since CH_4 is a strong absorber in this bandpass. Similarly, a reduction in the mixing ratio of CO allows observations to probe deeper at 4.5 μm, down to generally higher temperatures, leading to an increase in flux.

We now consider how an enhancement of CH_4 and depletion of CO in HAT-P-2b's atmosphere, as compared to solar metallicity equilibrium values, might occur near the apoapse of its orbit. Work by Visscher (2012) explores CO/CH_4 interconversion timescales for both HAT-P-2b and CoRoT-10b using one-dimensional models. In our simulations we find an average vertical windspeed[7] near the 1 bar level of ∼0.6 m s^{-1}. To get a rough estimate of the vertical eddy diffusion coefficient, K_{zz}, we simply multiply the vertical wind speed by a relevant vertical length scale which we assume to be the scale height, H. From our simulations we estimate a value of $H \sim 33$ km, which when combined with our estimate of the average vertical windspeed translates into $K_{zz} \sim 2 \times 10^8$ cm^{-2} s^{-1} near the 1 bar level. We note that this simplistic method of estimating K_{zz} might overestimate the actual atmospheric diffusivity as was shown to be the case in simulations of HD 209458b in Parmentier et al. (2013). Our estimate of K_{zz} places HAT-P-2b in the regime where vertical mixing (as opposed to orbit-induced thermal variations) is the dominant quenching mechanism according to Visscher (2012), which would result in a CH_4 mixing ratio of ∼10 ppm near the apoapse of HAT-P-2b's orbit.

One should also consider the possibility of horizontal transport as a possible source of disequilibrium carbon chemistry in HAT-P-2b's atmosphere. Such studies have been performed for HD 209458b by Cooper & Showman (2006) and Agúndez et al. (2012). As can be seen in Figures 3 and 4 a strong eastward equatorial jet is present in our simulations of HAT-P-2b near the apoapse of its orbit. The windspeeds in this zonal jet are ∼3500 m s^{-1} near the 1 bar level. Assuming that a horizontal dynamical timescale can be estimated as $\tau_{\rm dyn,h} = 2\pi R_p/U$, where R_p is the radius of the planet and U is the zonal windspeed, we estimate $\tau_{\rm dyn,h} \sim 10^5$ s. This horizontal dynamical timescale is significantly shorter than the timescale for conversion of CO to CH_4 (∼10^{10} s), and as found by Cooper & Showman (2006) and Agúndez et al. (2012) would likely result

[7] See Lewis et al. 2010, for more details on the determination of vertical wind speeds from the SPARC model.

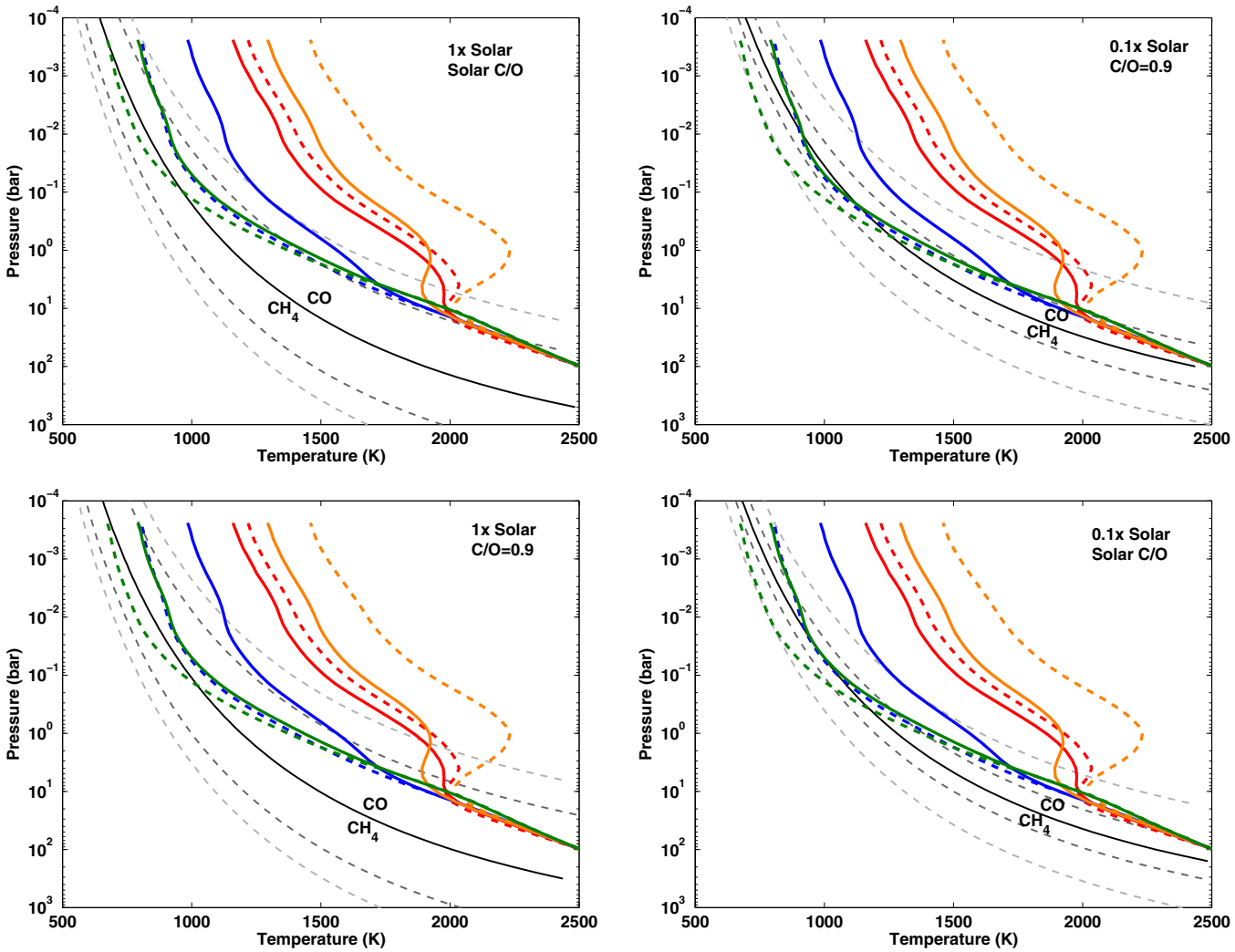

Figure 11. Globally averaged (solid lines) and Earth-facing hemisphere averaged (dashed lines) pressure temperature profiles from our atmospheric model taken near secondary eclipse (red), periapse (orange), transit (blue), and apoapse (green) compared with CO and CH_4 abundance contours assuming solar and 0.1× solar metallicity as well as C/O=0.55 (solar) and C/O=0.9 atmospheric compositions. In each panel the solid black line represents the CO=CH_4 contour. The dashed dark gray contours represent the 10 ppm CO (to the left of the solid line) and 10 ppm CH_4 (to the right of the solid line) contours. The dashed light gray contours represent the 1 ppm CO (to the left of the solid line) and 1 ppm CH_4 (to the right of the solid line) contours.

(A color version of this figure is available in the online journal.)

in a global enhancement of CO. Overall, it seems unlikely disequilibrium chemistry effects, either via horizontal or vertical quenching, are responsible for the discrepancies between our models and the observations of HAT-P-2b.

A significant deviation in the composition of HAT-P-2b's from the assumed solar composition could partially explain the differences between the theoretical and observed light curves at 3.6 and 4.5 μm. Figure 11 compares globally and Earth-facing hemisphere averaged pressure–temperature profiles from our simulations near secondary eclipse, transit, periapse, and apoapse with CO and CH_4 mixing ratios for various atmospheric compositions. In Figure 11 we have focused on cases where the atmospheric metallicity is reduces and/or an enhancement of the C to O ratio compared to solar values is assumed since this would naturally cause a depletion in the CO abundance of the planet (Moses et al. 2013b; Visscher 2012). The CO mixing ratio could be reduced to as low as 1 ppm at 100 mbar and 10 ppm at 1 bar on the Earth-facing hemisphere near apoapse if an atmospheric metallicity of 0.1× solar is considered. An atmospheric metallicity of 0.1× solar might seem extreme, but atmospheric chemistries far beyond what is commonly seen in our solar system have been proposed for a number of planets (e.g., Moses et al. 2013a, for GJ 436b).

5. CONCLUSIONS

We present a three-dimensional atmospheric circulation model for HAT-P-2b that incorporates realistic radiative transfer and equilibrium chemical processes for a range of atmospheric compositions and assumed rotation rates. Our atmospheric models reveal the complex radiative and dynamic processes that shape the phase curve of HAT-P-2b as observed at 3.6, 4.5, and 8.0 μm by Lewis et al. (2013). Although the 3.6 and 8.0 μm observations strongly favor models that include a thermal inversion near the periapse of HAT-P-2b's orbit, the exact timing of the peak in the planetary flux at 3.6, 4.5, and 8.0 μm cannot be explained by a single atmospheric model. It is likely that processes such as disequilibrium chemistry or pressure dependent drag effects, or an atmospheric composition that deviates significantly from solar abundances, could further align our predicted

phase curves with those we observed in Lewis et al. (2013). We also find the observed planetary fluxes near apoapse at 3.6 and 4.5 μm deviate from our model predictions, which suggest a possible variation in CO/CH_4 ratio from solar values.

Further work regarding the evolution of HAT-P-2b's atmospheric chemistry throughout its orbit is needed to fully explain our observations of HAT-P-2b. We plan to test how variations in the C/O ratio as well as a possible sub-solar metallicity composition for HAT-P-2b's atmosphere would affect global circulation patterns and theoretical phase variations. Additionally, we plan to include both CO/CH_4 chemistry and simple condensate cycles, including a self-consistent three-dimensional treatment of sources, sinks, and advection of these species with the atmospheric circulation. This will allow for an assessment of the effects of chemistry and cloud formation on the atmospheric structure and observables. Initial steps for the incorporation of chemical tracers in the SPARC model were taken by Parmentier et al. (2013) for the case of TiO in the atmosphere of HD 209458b, which is on a circular orbit. In addition to disequilibrium carbon chemistry, further transit, eclipse, and phase measurements of the HAT-P-2 system over a greater wavelength range would help to better constrain the chemistry of HAT-P-2b and provide insights into the nature of the dayside inversion as well as the carbon chemistry.

One key result from this study is that both observations and atmospheric models for HAT-P-2b support a short radiative timescale ($\sim$2 hr) near the infrared photosphere of HAT-P-2b near periapse. This measure of the radiative timescale can be used to help inform atmospheric models of planets in circular orbits in a similar temperature range, such as HD 209458b. Further observations of the HAT-P-2 system at 3.6 and 4.5 μm have been obtained using *Spitzer*. These observations will help us to further refine the exact timing in the peak of the planetary flux and allow us to create a two-dimensional dayside map of the planet at 4.5 μm. As we expand beyond the realm of close-in hot Jupiters into more Earth-like worlds questions regarding the habitability of planets on eccentric orbits will certainly arise. By refining our understanding of exoplanets like HAT-P-2b we will be able to use that knowledge to constrain the possible circulation, thermal, and chemical processes at work in other exoplanet atmospheres.

This work was performed in part under contract with the California Institute of Technology (Caltech) funded by NASA through the Sagan Fellowship Program executed by the NASA Exoplanet Science Institute. A.P.S. was supported by NASA Origins grant NNX12AI79G. M.S.M. acknowledges support from the NASA PATM program. N.K.L. wishes to thank C. Visscher for valuable discussions regarding possible chemical processes at work in HAT-P-2b's atmosphere. The authors thank the anonymous referee for their valuable comments on the manuscript.

REFERENCES

Adcroft, A., Campin, J.-M., Hill, C., & Marshall, J. 2004, MWRv, 132, 2845
Agúndez, M., Venot, O., Iro, N., et al. 2012, A&A, 548, A73
Amundsen, D. S., Baraffe, I., Tremblin, P., et al. 2014, A&A, 564, A59
Bakos, G. Á., Kovács, G., Torres, G., et al. 2007, ApJ, 670, 826
Cho, J. Y.-K., Menou, K., Hansen, B. M. S., & Seager, S. 2008, ApJ, 675, 817
Cooper, C. S., & Showman, A. P. 2005, ApJL, 629, L45
Cooper, C. S., & Showman, A. P. 2006, ApJ, 649, 1048
Cowan, N. B., & Agol, E. 2011, ApJ, 726, 82
Dobbs-Dixon, I., Agol, E., & Burrows, A. 2012, ApJ, 751, 87
Dobbs-Dixon, I., Cumming, A., & Lin, D. N. C. 2010, ApJ, 710, 1395
Fortney, J. J., Cooper, C. S., Showman, A. P., Marley, M. S., & Freedman, R. S. 2006, ApJ, 652, 746
Fortney, J. J., Lodders, K., Marley, M. S., & Freedman, R. S. 2008a, ApJ, 678, 1419
Fortney, J. J., Marley, M. S., Lodders, K., Saumon, D., & Freedman, R. 2005, ApJL, 627, L69
Fortney, J. J., Marley, M. S., Saumon, D., & Lodders, K. 2008b, ApJ, 683, 1104
Freedman, R. S., Marley, M. S., & Lodders, K. 2008, ApJS, 174, 504
Fu, Q., & Liou, K. N. 1992, JAtS, 49, 2139
Goody, R., West, R., Chen, L., & Crisp, D. 1989, JQSRT, 42, 539
Guillot, T. 2005, AREPS, 33, 493
Heng, K. 2012, ApJL, 761, L1
Heng, K., Menou, K., & Phillipps, P. J. 2011, MNRAS, 413, 2380
Hubeny, I., Burrows, A., & Sudarsky, D. 2003, ApJ, 594, 1011
Hut, P. 1981, A&A, 99, 126
Kataria, T., Showman, A. P., Lewis, N. K., et al. 2013, ApJ, 767, 76
Knutson, H. A., Charbonneau, D., Allen, L. E., et al. 2007, Natur, 447, 183
Knutson, H. A., Charbonneau, D., Cowan, N. B., et al. 2009, ApJ, 690, 822
Knutson, H. A., Lewis, N., Fortney, J. J., et al. 2012, ApJ, 754, 22
Langton, J., & Laughlin, G. 2007, ApJL, 657, L113
Langton, J., & Laughlin, G. 2008, ApJ, 674, 1106
Laughlin, G., Deming, D., Langton, J., et al. 2009, Natur, 457, 562
Lewis, N. K., Knutson, H. A., Showman, A. P., et al. 2013, ApJ, 766, 95
Lewis, N. K., Showman, A. P., Fortney, J. J., et al. 2010, ApJ, 720, 344
Liu, B., & Showman, A. P. 2013, ApJ, 770, 42
Lodders, K. 2002, ApJ, 577, 974
Lodders, K., & Fegley, B. 2002, Icar, 155, 393
Lodders, K., & Fegley, B. Jr. 2006, in Chemistry of Low Mass Substellar Objects, ed. J. W. Mason (Berlin: Springer), 1
Loeillet, B., Shporer, A., Bouchy, F., et al. 2008, A&A, 481, 529
Marley, M. S., & McKay, C. P. 1999, Icar, 138, 268
Mayne, N. J., Baraffe, I., Acreman, D. M., et al. 2014, A&A, 561, A1
Menou, K., & Rauscher, E. 2009, ApJ, 700, 887
Mlawer, E. J., Taubman, S. J., Brown, P. D., Iacono, M. J., & Clough, S. A. 1997, JGR, 102, 16663
Moses, J. I., Line, M. R., Visscher, C., et al. 2013a, ApJ, 777, 34
Moses, J. I., Madhusudhan, N., Visscher, C., & Freedman, R. S. 2013b, ApJ, 763, 25
Murray, C. D., & Dermott, S. F. (ed.) 1999, Solar System Dynamics (New York: Cambridge Univ. Press)
Pál, A., Bakos, G. Á., Torres, G., et al. 2010, MNRAS, 401, 2665
Parmentier, V., Showman, A. P., & Lian, Y. 2013, A&A, 558, A91
Perez-Becker, D., & Showman, A. P. 2013, ApJ, 776, 134
Perna, R., Heng, K., & Pont, F. 2012, ApJ, 751, 59
Rauscher, E., & Menou, K. 2010, ApJ, 714, 1334
Rauscher, E., & Menou, K. 2013, ApJ, 764, 103
Showman, A. P., Cho, J. Y.-K., & Menou, K. 2010, in Atmospheric Circulation of Exoplanets, ed. S. Seager (Tucson, AZ: Univ. Arizona Press), 471
Showman, A. P., Cooper, C. S., Fortney, J. J., & Marley, M. S. 2008, ApJ, 682, 559
Showman, A. P., Fortney, J. J., Lewis, N. K., & Shabram, M. 2013, ApJ, 762, 24
Showman, A. P., Fortney, J. J., Lian, Y., et al. 2009, ApJ, 699, 564
Showman, A. P., & Guillot, T. 2002, A&A, 385, 166
Showman, A. P., & Polvani, L. M. 2011, ApJ, 738, 71
Sing, D. K., Lecavelier des Etangs, A., Fortney, J. J., et al. 2013, MNRAS, 436, 2956
Visscher, C. 2012, ApJ, 757, 5
Winn, J. N., Johnson, J. A., Peek, K. M. G., et al. 2007, ApJL, 665, L167